Title
EXPERIMENTAL ANALYSIS OF PORE BREAKAWAY FROM TWO GRAIN JUNCTIONS

Author
Sakarcan, M.

Publication Date
1981-12-01

Lawrence Berkeley Laboratory

UNIVERSITY OF CALIFORNIA

Materials & Molecular Research Division

EXPERIMENTAL ANALYSIS OF PORE BREAKAWAY FROM TWO GRAIN JUNCTIONS

Metin Sakarcan
(M.S. thesis)

December 1981

Prepared for the U.S. Department of Energy under Contract DE-AC03-76SF00098

DISCLAIMER

EXPERIMENTAL ANALYSIS OF PORE BREAKAWAY FROM TWO GRAIN JUNCTIONS

Metin Sakarcan

M.S. Thesis

December 1981

Lawrence Berkeley Laboratory
University of California
Berkeley, CA 94720

This work was supported by the Director, Office of Energy Research, Office of Basic Energy Sciences, Materials Sciences Division of the U.S. Department of Energy under Contract No. DE-AC03-76SF00098.

EXPERIMENTAL ANALYSIS OF PORE BREAKAWAY FROM TWO GRAIN JUNCTIONS

CONTENTS

EXPERIMENTAL ANALYSIS OF PORE BREAKAWAY FROM TWO GRAIN JUNCTIONS

Metin Sakarcan

ABSTRACT

Pore breakaway from two grain junctions in MgO has been experimentally studied. Breakaway was induced by heat treating hot pressed specimens with residual porosity. Scanning electron microscopy was used to determine pore and grain boundary morphologies at various stages of breakaway. Changes in pore shapes were related to calculated differences in velocities between the leading and trailing pore surfaces. A comparison of the boundary velocity in the vicinity of a dragging pore with the average pore velocity indicated that the remote boundary velocity exceeds the pore velocity. The mobility ratio, $D_s\delta_s/M_b$, necessary to maintain pore-grain boundary attachment was estimated. This ratio was then used in conjunction with measurements of the intragranular pore size distribution to substantiate the existance of a critical pore size for pore-grain boundary separation.

1. INTRODUCTION

Ceramics and other high temperature materials are often produced by sintering; during which both densification and grain growth occur. The goal of sintering science is to develop a basis (i.e., through the construction of sintering maps) for specifying optimum sintering conditions, i.e., those which maximize the degree of densification and minimize the extent of grain growth. Many such studies have been performed focussing on the effect of process variables such as, additives, atmosphere and particle size distribution on the final microstructure. Proper adjustments of the process variables tailors the optimum final stage microstructure of ceramics; the final properties of the finished article being strongly dependent on the grain size, pore size and the size distributions.

The grain size generally affects the properties of ceramic products either, because it determines the length over which some parameter accumulates (for example, the extent of the mismatch between grains arising from anisotropic thermal expansion) or because it dictates the frequency with which grain boundaries and their different properties (such as, mass transport) are encountered. Few properties of ceramics are completely independent of grain size, however, most attention has been focussed on those properties for which clear structure-grain size-property relationship exist. For example, the size of inherent flaws and the length of dislocation pile-ups leading to fracture can be grain size related (Carneglia, 1972; Davidge and Evans, 1970). The predominant mechanism operating during high temperature creep deformation can involve diffusional creep or grain boundary sliding (Heuer, 1970): both

processes exhibit appreciable grain size dependences. Generally, for properties where hysterisis loops are observed, as in ferrimagnets and ferroelectrics, the importance of the grain size can be interpreted in terms of the existance of domain walls and the effect of interactions with grain boundaries on the ease of wall migration (Brooks, 1976). Below a certain grain size (which depends on the nature of the material) domains cannot form, and hard magnetic properties in ferrites and high dielectric constants in ferroelectrics are observed. Grain boundaries can have a pronounced effect on electrical conductivity in ceramics since they can adjust more readily to changing conditions (equilibration in terms of either temperature and composition) than can the grain interiors. This effect is perhaps most pronounced in semiconducting $BaTiO_3$, where the occurrence of oxygen absorption at the grain broundaries introduces a high resistance barrier to electrical conduction (Heywang, 1971). Control of grain size can then be used as a means of increasing the concentration of such barriers, thus making the system more resistant to electrical breakdown (Hirose and Sasaki, 1971).

Another motivation for controlling grain growth is due to its potentially deleterious effect on both the densification rate and the final density which can be achieved by sintering (Coble and Burke, 1963). Densification can only proceed at a reasonable rate as long as the sources and the sinks for the associated diffusion process are in close proximity. Further, the identification of the grain boundary and the pore as the sources and the sinks for the diffusing atoms suggests that theoretical density is only to be expected when pores remain attached to grain boundaries (Burke, 1957).

It is thus necessary to control the rate and/or extent of grain boundary motion such that pore-boundary attachment is maintained. The available control techniques constitute either decreasing the grain boundary mobility or increasing the densification rate such that the time available for grain growth is appreciably reduced. The study undertaken here deals with the nature of boundary motion in the presence of pores in nominally pure MgO.

During the sintering process, pores located on grain boundaries simultaneously shrink and coalesce. However, circumstances can arise which cause boundaries to separate from pores; thereby, discouraging the densification process (Sosmon lecture, Evans, 1979). Specifically, pores attached to grain boundaries shrink by a grain boundary diffusion process but once detached, shrink by the (usually) much slower mechanism of lattice diffusion (Hsueh and Evans, 1981). Consequently prolonged sintering times are necessary for further densification resulting in further and generally undesirable grain growth.

Previous studies (Brook, 1969 and Carpay, 1977) in this area have introduced simplified concepts of the physical interactions between the pore and grain boundary during breakaway. The final result of these analyses can be expressed in terms of a separation diagram in pore, grain size space as illustrated in Figure 1 (Carpay, 1977). Another very recent analysis (Hsueh and Evans, 1981) has emphasized the physical mechanisms involved in the separation process, and thereby identified several quantitative features of the separation diagram (Fig. 2) (Spears and Evans, 1981).

The Brook-Carpay analysis is essentially based upon solutions for the interaction of a boundary with a rigid second phase particle.

Specifically, the interaction between a pore and a moving grain boundary assumes a spherical pore moving through an isotropic homogeneous material at some velocity (Fig. 6) determined by the surface diffusivity.

The force, F, dictating separation is derived for the spherical pore by assuming that the contact line between the boundary and the pore can move freely over the pore surface (Fig. 6); whereupon the force becomes:

$$F = 2\pi a_o \gamma_b \cos\theta \sin\theta \tag{1}$$

where θ is the boundary intersection angle, γ_b is the grain boundary energy and a_o is the pore radius. The force has a maximum value $\hat{F}$ at $\theta = \pi/4$ given by

$$\hat{F} = \pi a_o \gamma_b \tag{2}$$

This force maximum coupled with the pore mobility, M_p:

$$M_p = \frac{D_s \delta_s \Omega}{kT\pi a_o^4} \tag{3}$$

yields a peak pore velocity, $\hat{V}_p$:

$$\hat{V}_p = M_p \hat{F}_p = \frac{\Omega D_s \delta_s \gamma_s}{kT\, a_o^3} \tag{4}$$

where Ω is the atomic volume (of MgO), and $D_s\delta_s$ is the surface diffusion parameter. Breakaway is considered to occur when the grain boundary velocity exceeds this peak pore velocity (Brook, Carpay, Hsueh and Evans).

The more recent model (Hsueh and Evans, 1981) addresses a physical description of the attached pore motion. Pore shapes are lenticular for stationary boundaries and of constant volume during motion. The driving force is the chemical potential gradient which arises from the difference in radius of curvature along the surface. The force maximum in this circumstance occurs when the pore attains a maximum steady state velocity, $\hat{V}_p$. Breakaway is deduced from a comparison of the peak steady state pore velocity, $\hat{V}_p$, with the nearby boundary velocity, V_b. Adopting this criterion, pore separation is shown to occur whenever the pore size, a, exceeds a critical value, independent of the grain size given by:

$$a_c^2 = (1/\sqrt{3})(\Omega^{1/3} D_s \delta_s / kTM_b)(17.9 - 6.2\psi)/\cos \psi/2 \qquad (5)$$

where ψ is the dihedral angle (Fig. 3) and M_b is the boundary mobility. However, the analysis neglects the detailed processes that accompany the non-steady state progression of the pore, grain boundary ensemble to eventual breakaway.

The present study has examined several aspects of the Hsueh and Evans model. The morphologies of pores attached to grain boundaries were examined. Some of the observed shapes were consistent with those predicted (Hsueh and Evans) for steady state pore motion. In addition, pore morphologies presumably corresponding to non-steady state motion at velocities exceeding the steady state maximum were also observed. The characteristics of the pore shapes were used to assess the validity of the the aspects of the theory dealing with pore-grain boundary distortions and the existence of the steady state maximum pore velocity. Information of this type should provide an eventual basis for analysing non-steady-state behavior and thereby performing rigorous calculations.

Secondly, the dimensions of separated pores, contained within grains were measured and used to assess the approximate validity of the critical pore size predicted by eqn. (5). This was achieved by estimating the relative mobilities of pores attached to grain boundaries and then computing the magnitude of $D_s\delta_s/M_b$ (by equating the pore and boundary velocities at the attachment locations); coupled with independent determinations of the grain boundary mobility (from grain growth data obtained on 90-95% dense polycrystals) and an assessment of the pore size distribution at separation (by equating the intergranular pore coarsening).

The implications of the results to final state sintering are then discussed.

---

†A pore at a non-steady-state develops a velocity gradient, that is, the velocity of pore surfaces are position dependent with a maximum at the axis of the leading surface.

2. EXPERIMENTAL

2.1 EXPERIMENTAL PROCEDURES

The material used for the present study was an undoped MgO purchased from Mallincrodt Chemical Company (refer to Table II for the chemical analysis). The original particle size ranged from 1 to 3 μm.

The powder was calcined and vacuum hot pressed (10^{-4} torr) in a graphite die. Hot pressing temperatures ranged from 1200 to 1300°C with pressures ranging from 177×10^5 to 354×10^5 NM^{-2}. The pressure was relased immediately after shrinkage was essentially complete at the subject pressure and temperature.

The hot pressing temperature and pressures were selected to achieve final stage microstructures (i.e., isolated pores). Following the hot pressing the surfaces were removed by mechanical procedures and the center regions were inspected for pore breakaway events. Specimens were later roughly polished using SiC paper and further heat treated at higher temperature (1500°C) for times ranging between 1 and 24 hours to induce pore-grain boundary separation. Subsequent fine polishing procedures were conducted using diamond paste (6 μm) and Al_2O_3 powder (0.3 μm). Specimens were thermally etched in air (1450°C) for 30 minutes and then examined using optical and scanning electron microscopy.

In addition to morphological observations, measurements of intragranular pore and grain sizes were made on polished sections following consecutive firing processes. The average radii of the intragranular pores were calculated from the distributions of the circular pores measured from SEM micrographs; while average grain size measurements were conducted using optical micrographs.

2.2 MORPHOLOGICAL OBSERVATIONS

Scanning electron microscopy studies were performed on fractured surfaces in order to observe the shape of a dragging pore in three dimensions. Figure 5 depicts the morphology of such pores (indicated by arrows). Subsequent observations were performed on polished surfaces, were confined to two dimensions. A schematic of pore shapes identified from SEM micrographs (Fig. 8) shows the changes occurring during the breakaway process while, scanning electron micrographs of actual pores having a similar sequence of morphologies are shown in Figure 9. The progression of the leading surface from a concave to convex shape is evident. Comparison of individual micrograph with these predicted pore shapes indicated that the first three of the micrographs (Fig. 9) are similar to the ones below the steady-state maximum, however, pore shapes significantly differing were also observed. Since the pores located, in the sequence, between the pore with maximum steady state pore velocity (8-C) and the isolated pore are different as compared to the predicted pore shapes; therefore, they must represent the "non-steady-state" pore shapes. As noted in the previous sections, pore and boundary shapes, in sequence during the separation event are characterized by their two curvatures; the in-plane radius of curvature, R_1, and the axisymmetric curvature, R_2. When the pore velocity exceeds the steady state maximum, the boundary out-of-plane radius of cruvature, R_2, decreases continuously, diminishing the pore contact radius, a, and thereby permitting the occurrence of the separation as shown in Figure 9.

3. RESULTS

3.1 THE THEORETICAL BASIS

The motion of pores with grain boundaries is achieved by inducing a flux of atoms from the leading to the trailing surface of the pore (Fig. 3). The driving force for the atom flux is associated with the existence of a gradient in the curvature of the pore surface. Pore distortion is thus a necessary consequence of pore motion. The pore velocity is in turn the consequence of pore distortion.

The pore shape (Fig. 4) can be represented by the two curvatures; an in-plane radius of curvature, K_1, and an axisymmetric radius of curvature, K_2 (Fig. 4) (Hsueh and Evans)

$$K_1 = (d^2y/dx^2)[1 + (dy/dx)^2]^{-3/2} \tag{6}$$

$$K_2 = 1/x(dy/dx)[1 + (dy/dx)^2]^{-1/2} \tag{7}$$

where x and y are the coordinates of the pore surface. For a given pore shape (x, y) the curvatures can be calculated as a function of x from equations (6) and (7). Thus the chemical potential, proportional to the sum of the curvatures ($\mu_o = 0$) can be related to the pore shape (Hsueh and Evans).

The flux, J_s, of atoms can subsequently be determined from the curvature gradient using (Hsueh and Evans),

$$J_s = \left(\frac{D_s\delta_s\gamma_s}{kT}\right)\frac{d(K_1 + K_2)}{dx}\left(1 + (dy/dx)^2\right)^{-1/2} \equiv \frac{BD_s\delta_s\gamma_s}{kT} \tag{8}$$

where γ_s is the surface energy and $D_s\delta_s$ is the surface diffusivity. Finally the velocity V_p of the pore in the axial (y) direction can be calculated from the flux, using the finite difference relation (Hsueh and Evans)

$$V_p = 2\Omega\left(\frac{J_1X_1 - J_2X_2}{X_1^2 - X_2^2}\right) \equiv \frac{\Omega D_s\delta_s\gamma_s}{kT}(\Delta\beta/\Delta X) \qquad (9)$$

where X_1 and X_2 are the surface locations for the fluxes J_1 and J_2, respectively.

The same reasoning can be applied to the grain boundary velocity. The driving force originating from the curvature gradient can be expressed (Hsueh and Evans, 1981) as:

$$F_b = \gamma_b\Omega^{2/3}(1/R_1 + 1/R_2) \qquad (10)$$

where γ_b is the boundary energy. For the dragging pore, the in-plane radius of curvature, K_1, is negative. However, a driving force with a component acting in the direction of pore velocity still exist whenever the out-of-plane curvature $R_2 < |R_1|$. The existence of the out-of-plane curvature accounts for the observed motion of pores away from their in-plane center of curvature.

The velocity of the boundary (subject to pore drag) is the product of boundary mobility and the driving force. Thus the boundary velocity, V_b, in the axial direction becomes

$$V_b = M_b\gamma_b\Omega^{2/3}(-1/R_1 + 1/R_2)\left(1 + (dy/dx)^2\right)^{-1/2} \equiv M_b\gamma_b\Omega^{2/3}\xi \qquad (11)$$

where the last term in parantheses accounts for the component velocity,

v_b^n, in the axial direction. When boundary velocity, V_b, exceeds the pore velocity, V_p, the component boundary velocity induces unstable boundary motion by decreasing the magnitude of R_2 in excess of the change in R_1. This is accompanied by a marked decrease pore contact radius, a, and convergence of the boundary onto the pore axis becomes inevitable.

Once the pore and boundary velocities are known, information can be gained about the mechanisms of separation. Furthermore, the surface diffusivity to boundary mobility ratio, $D_s\delta_s/M_b$, can be calculated from pore and boundary velocities and compared (Appendix I) with independently determined values.

3.2 THE RELATIVE PORE VELOCITY

To understand the motion of pores with grain boundaries the relative local velocities were calculated through measurements of pore shapes. For a small pore ($\bar{<}r$ = 0.5 - 0.7 μm for MgO), at 1500°C, surface diffusion is the dominant atom transport mechanism (Hsueh and Evans). Pore motion occurs when atoms are transported from the leading to the trailing pore surface by surface diffusion. This process requires that the chemical potential at the leading surface exceed that at the trailing surface. The pore shapes yield information concerning the chemical potential gradient along the pore surfaces (eqns. 6 and 7), as depicted in Figure 10 for the leading (A) and the trailing (B) of a typical pore. Figure 10 indicates that the basic chemical potential requirement for pore motion is satisfied for the pore depicted in Figure 9-4.

The atom flux required for pore motion was deduced by taking the gradient of the sum of the two curvatures, as plotted in Figure 12. The

opposing flux directions (as predicted) associated with the leading and trailing surfaces are indicative of the motion of surfaces in the same direction (the atom flux leaves the leading and enters the trailing surface).

The velocities associated with these two surfaces were calculated (Appendix III) from the atom flux at each point over the pore surfaces (eqn. 9). Average values of the velocities thus calculated were compared for the leading and the trailing surfaces. For "non-steady-state" pore shapes, the leading surfaces are invariably calculated to move significantly faster than the trailing surfaces, by a factor >2; thereby satisfying the conditions for non-steady-state motion. For steady state pore shapes significant velocity differences were not evident, as predicted by the theory (Hsueh and Evans, 1981).

3.3 THE GRAIN BOUNDARY MOBILITY

The time dependence of the average grain size was determined on dense (90-95% of the theoretical value) specimens using (Fullman, 1953),

$$\bar{G} = \frac{L}{N.M}\,(1.5) \qquad (12)$$

where L is the total length of the random lines, N is the number of intercepts and M is the magnification. Average grain sizes thus measured were used to calculate the average boundary mobility at 1500°C (M. F. Yan, 1976)

$$\bar{G}^2 - \bar{G}_o^2 = 2\bar{M}_b\gamma_b t\Omega^{2/3} \qquad (13)$$

where $\bar{G}$ and $\bar{G}_o$ are the average grain sizes after and before the heat treatment. The value of the average boundary mobility was estimated

($M_b\Omega^{2/3} = 2.7 \times 10^{-15}$ cm^3 dyn^{-1} s^{-1}) from the slope of the plot depicted in Figure 7-a and compared with that in literature ($M_b\Omega^{2/3} \cong 10^{-11}$ cm^3 dyn^{-1} s^{-1}). This large difference ($\sim 10^4$) between the two results may be either due to solute drag from impurities in the starting powder (Table 2) or due to the drag exerted by the pores within the hot pressed compacts.

The values for the average boundary mobility (experimental and literature) were used in assessing the velocity of individual boundaries attached to pores (Fig. 9). The necessary driving force originates from the boundary curvature, defined previously. A gradient in the driving force results in a position dependent boundary velicity and accounts for a change in grain boundary shape (average boundary mobility was used at every point along the boundary). Measurements of the boundary curvature† were used to estimate the driving force (eqn. 10) within the influence zone (Fig. 4). The results are plotted as a function of X in Figure 13. The boundary velocity could then be calculated from the driving force eqn. (11).

For a pore to move along with the boundary, equality of the pore and boundary velocities is required. Using the velocities of each specified pore and the attached boundary, a value for the surface diffusivity to grain boundary mobility ratio can be estimated (Appendix I) as, $D_s\delta_s/M_b = 8 \times 10^{-24}$ Nm^2. The value for this ratio calculated by direct substitution of the parameters ($D_s = 3 \times 10^{-11}$ m^{2}s^{-1},

†In calculating the driving forces for pore and/or grain boundary motion due to curvature, from morphologies in planar sections, it is assumed that the axis of cylindrical symmetry of the pore lies within the plane of polish.

δ_s = 2.65 x 10^{-10}m (Lytle and Stubican) and $M_b\Omega^{2/3}$ = 10^{-10} $m^3N^{-1}s^{-1}$ (M. F. Yan)) is 5 x 10^{-30} Nm^2. A surface diffusivity estimate, $D_s\delta_s$ = 3 x 10^{-18} m^3s^{-1}, obtained from the mobility ratio using M_b deduced from the grain growth results compares with a literature value of $D_s\delta_s$ = 7 x 10^{-21} m^3s^{-1}. This discrepancy may suggest that the small scale surface diffusivity pertinent to small pores may exceed the values obtained from macroscopic measurements; similar to the boundary diffusivity trends implied from sintering studies in Al_2O_3 (Coble et al.).

3.4 THE INTRAGRANULAR PORE SIZE DISTRIBUTION

The cross-sectional pore radius distribution f(r) dr determined from polished sections was plotted as a function of annealing time and then converted to the actual pore radius distribution, F(a) da, using (Fullman and Cahn, 1956),

$$\pi a F(a) = \int_{\infty}^{a} (r^2 - a^2)^{-1/2} f^1(r)\, dr \qquad (14)$$

where a is the spherical pore radius and r is the circular pore radius. A resultant cumulative pore radius distributions F(R) are plotted in Figure 14).

The time dependence of the pore size at 1500°C is plotted in Figure 7-b. The increase in intragranular pore size over the range of 1 to 24 hours suggests that the pores coarsen by lattice diffusion (Appendix II) (rather than by grain boundary pick-up and the resultant coarsening by grain boundary diffusion or coalescence). The intragranular pore size distribution at separation is probably, therefore, most closely described by the short time distribution given in Figure 15.

3.5 THE CRITICAL PORE SIZE

The consistency of the measurements and the validity of the critical pore size prediction given by eqn. (5) can be simultaneously assessed by inserting the magnitude of $D_s\delta_s/M_b$ deduced in a prior section and evaluating the dihedral angle distribution from the pore radius distribution. For this first critical pore sizes corresponding to each dihedral angle over the range of 0 to 180° was calculated using eqn. (5). Secondly, the resultant cumulative and frequency distributions of the dihedral angle corresponding to each point over the short time intergranular pore size distribution (Fig. 14) were determined and plotted in Figures 15 and 16, respectively. Inspection of Figure 16 reveals a reasonable spectrum of dihedral angles, ψ: with the center of the distribution occurring within the permissible range, i.e., between the lower limit for sintering 70° and 180°. Additionally, the median value (155°) is close to the value (150°) typically quoted for oxides.

4. IMPLICATIONS AND CONCLUSION

Pore breakaway from two grain junctions has been experimentally studied for the first time using MgO. Specimens were made by hot pressing and later heat treated to induce breakaway. Fine polished specimens were examined using scanning electron microscopy in order to characterize the morphologies of the pores and grain boundaries. Velocities of the associated pore and boundary were calculated through measurements of the boundary shapes.

Distortions of the pores with increasing boundary velocity (Fig. 8) are a consequence of pore motion with the boundary. Velocities calculated from the pore shapes indicated that non-steady-state behavior exists at high pore velocities such that the leading pore surface propagates at a more rapid rate than the trailing surface; whereas steady state prevails at low velocities. These observations are in qualitative accord with theoretical predictions.

A study of the size distribution of pores entrapped within grains has been used to investigate the validity of the theoretical pore, grain boundary breakaway predictions. This is achieved by independently estimating the mobility ratio, $D_s\delta_s/M_b$, from studies of pore shapes. The results of the analysis are expressed in terms of a distribution of dihedral angles predicted from the pore size distribution, the mobility ratio and the theoretical critical size. The predicted dihedral angle distribution lies within an acceptable range and exhibits a median value in close agreement with quoted values for oxides. The reasonable correlation provides a first order validation of the theoretically derived expression for the critical pore size.

Many additional, comparable studies are needed to critically evaluate the validity of the existing models and to suggest areas in which the models, which are still substantially simplified, require further attention. The particular emphasis placed in this study on the shapes of pores and the grain boundaries represents the first attempt to constructively use morphological information. The reasonable success achieved encourages further studies of the type expanded to include pores at three grain edges and two grain corners. Further studies of intergranular and intragranular pore size distributions should also provide valuable information.

ACKNOWLEDGEMENTS

I must express my deepest appreciation to all the outstanding people who gave me encouragement, insight and faith in making this work possible. In particular, I thank Professor Anthony G. Evans for his guidance and patience. Special thanks must be extended to Shu-Sheng Chiang, Chun-Hway Hsueh, Marlene Spears, Bill Blumenthal and all of the students and staff for their efforts and advice. Most of all, I thank Sümerbank for supporting me financially during my educations in the United States. This work was supported by the Director, Office of Energy Research, Office of Basic Energy Sciences, Materials Science Division of the U.S. Department of Energy under Contract No. DE-AC03-76SF00098.

REFERENCES

1. Carneglia, S. C. (1972), J. of Amer. Cer. Soc., 55, 243.
2. Davidge, R. W., Evans, A. G. (1970), Mat. Sci. Eng., 6, 281.
3. Heuer, A. H. (1970), Proc. British Ceram. Soc., 15, 173.
4. Brook, R. J. (1969), J. Amer. Ceram. Soc., 52, 56.
5. Heywang, W. (1971), J. Mater. Science, 6, 1214.
6. Hirose, N., Sasaki, H. (1971), J. Amer. Ceram. Soc., 54, 320.
7. Coble, R. L., Burke, J. E. (1963), Progr. Ceram. Sci., 3, 197.
8. Burke, J. E. (1957), J. Amer. Ceram. Soc., 40, 80.
9. Evans, A. G. (1981), Sasman Lecture.
10. Hsueh, C. H., Evans, A. G. (1981), Microstructure Development During Final Stage Sintering, to be published.
11. Carpay, F. M. A. (1977), J. Amer. Cer. Soc., 60, 82.
12. Spears, M. A., Evans, A. G. (1981), Microstructure Development During Final/Intermediate Stage Sintering, to be published.
13. Lytle, S. A., Stubican, V. S. (1981), Surface Diffusion in MgO and Cr-Doped MgO, M.S. Thesis, The Penn. State Univ.
14. Yan, M. F. (1976), Ceramic Microstructure, p. 276.
15. Fullman, R. L., Cahn, J. W. (1956), Trans. AIME, Journal of Metals, 610.
16. Fullman, R. L. (1953), Trans. AIME, 197 (3), 447.
17. Kingery, W. D. (1975), Introduction to Ceramics, 240.
18. Greenwood, G. W. (1956), Acta Metallurgica, 4 [3], 243.
19. Narayan, J., and Washburn, J. (1973), Acta Metallurgica, 21, 533.
20. Coble, R. L., Dynys, J. M., Coblenz, W. S., Cannon, R. M., Sintering Processes, edited by Kuczynski, G. C., Plenum Pub. Co.

FIGURE CAPTIONS

Fig. 1. The relation between the pore and the grain size as a schematic of separation and attachement regions.

Fig. 2. The relation between the critical pore size for separation a_c and the peak pore size $\hat{a}$.

Fig. 3. A schematic of a moving pore indicating the atom flux and the inclination of the grain boundary θ.

Fig. 4. The axisymetric configuration associated with pore drag, illustrating the important curvatures, the influence distance and the pore and the grain boundary velocities.

Fig. 5. Fractured surface of an MgO specimen illustrating shape of a dragging pore in three dimensions as shown by arrows.

Fig. 6. A schematic of a spherical pore attached to a grain boundary. The boundary is assumed to separate from the pore when θ is 45°.

Fig. 7.- a. Illustrates the change in grain size with time at 1500°C. Each data point represents the average value of the measurements done on four different specimens treated equally.

b. Illustrates the change in pore size with time at 1500°C. Each point is calculated from measurements of circular radii distribution of average of 200 pores from SEM micrographs with magnification ranging between 2000X to 5000X.

Fig. 8. A schematic of pore shapes, in sequence, associated with increasing boundary velocities a-c are the steady state pore shapes and d-g are the non-steady state pore shapes.

Fig. 9. Scanning electron micrographs of the pore shapes, in sequence associated with increasing boundary velocity; 1-3 are the steady state pore shapes and 4-8 are the non-steady state shapes.

Fig. 10. The relation (deduced from measurements of a non-steady state pore shapes) between the driving force and the position, X, over the pore surface, a - for the leading surface, b - for the trailing surface.

Fig. 11. A schematic of a pore in non-steady state motion illustrating the directions of pore motion as well as the velocity components.

Fig. 12. The relation between the atom flux of a pore in a non-steady state motion and the position, X, over the pore surface, a - for the leading surface, b - for the trailing surface.

Fig. 13. The relationship between the driving force of a boundary in a non-steady state motion and the position X over the boundary surface.

Fig. 14. Intragranular pore size cumulative distribution after firing 3, 6 and 12 hours at 1500°C.

Fig. 15. Cumulative distribution of the dihedral angle determined from the first cumulative intragranular pore size distribution.

Fig. 16. Frequency distribution of dihedral angle.

TABLE I

Time (Hrs)	Grain Radius (μm)	Pore Radius
0	4.4	0.315
3	7.75	0.525
6	12.8	0.60
12	17.5	0.775
24	24.0	0.945

TABLE II

(Chemical analysis of the powder used.
Maximum limits of impurities.)

Ammonium Hydroxide Ppt	0.02%
Barium (Ba)	0.005%
Calcium (Ca)	0.05%
Chloride (Cl)	0.01%
Heavy Metal (as Pb)	0.003%
Insoluble in Hcl	0.02%
Iron (Fe)	0.01%
Loss on ignition	2.0%
Manganese (Mn)	0.0005%
Nitrate (NO_3)	0.005%
Potassium (K)	0.005%
Sodium (Na)	0.5%
Soluble in water	0.4%
Strontium (Sr)	0.005%
Sulfate and sulfite (as SO_4)	0.015%

APPENDIX I

THE MOBILITY RATIO

The velocities of pore and boundary can be used to estimate the surface diffusivity to grain boundary mobility ratio. It is required that the velocities of pore and boundary be equal ($V_p = V_b$) for a pore to move along with the boundary. Hence, from equations (8), (9) and (11),

$$\frac{D_s\delta_s}{M_b} = \frac{kT\,\gamma_b}{D_s\delta_s\gamma_s\Omega^{1/3}}\,\frac{\xi}{(\Delta\beta/\Delta X)} \qquad \text{(A-1)}$$

By substituting the appropriate values for these parameters from the text the mobility ratio can be estimated as $D_s\delta_s/M_b = 8 \times 10^{-24}\ Nm^2$.

APPENDIX II

PORE COARSENING

On the assumption that intragranular pores coarsen by lattice diffusion, the time dependence of the pore radii should be given by (Greenwood, 1956),

$$a^3 - a_o^3 = \frac{6\Omega D_\ell \gamma_s t}{kT} \equiv \alpha t \qquad \text{(A-2)}$$

where a and a_o are the pore radii after and before firing, respectively, D_ℓ is the lattice diffusivity and t is the time. By plotting $(a^3 - a_o^3)$ from Table I (Fig. 7-b) as a function of time a value for α can be estimated from the slope. The lattice diffusivity estimated by inserting the appropriate values of the other parameters is $D_\ell = 2.2 \times 10^{-18}$ m^2s^{-1}. This compares with the anion diffusivity at the same temperature of $D_\ell^o = 10^{-17}$ m^2s^{-1}, a cation diffusivity of $D_\ell^{Mg} = 10^{-14}$ m^2s^{-1} (Kingery) and a pipe diffusivity rate for anion of $D_{pipe}^o = 10^{-20}$ m^2s^{-1} (Narayan and Washburn).

APPENDIX III

CALCULATION OF PORE VELOCITY AT A POINT OVER THE PORE SURFACE

Using Figure 12, the last two terms (β) of the flux equation (7) can be obtained as a function of X. For the two closest points over the pore surface (for the leading surface) the values of β are,

$$\beta_6 \cong -0.7 \times 10^3 \ m^{-2}$$

$$\beta_8 \cong -1.2 \times 10^3 \ m^{-2}$$

where the subscripts of β refer to the positions (X) along the pore surface. Thus the actual value of the atom fluxes for these two positions can be estimated using the following choices for the flux parameters,

$D_s \cong 3 \times 10^{-11} \ m^2 s^{-1}$ (Lytle and Stubican, 1980)

$\gamma_s \cong J/m^2$

$\delta_s = 2.65 \times 10^{-10} \ m$

$\Omega_{MgO} = 1.87 \times 10^{-29} \ m^3$

$k = 1.38 \times 10^{-23} \ J/°K$

$T = 1773°K$

By substituting the calculated flux values in eqn. (9) and multiplying by the cube of magnification (27000X), the leading surface velocity of the pore at the specified points can be found ($V_p^L = 5 \times 10^{-14} \ ms^{-1}$).

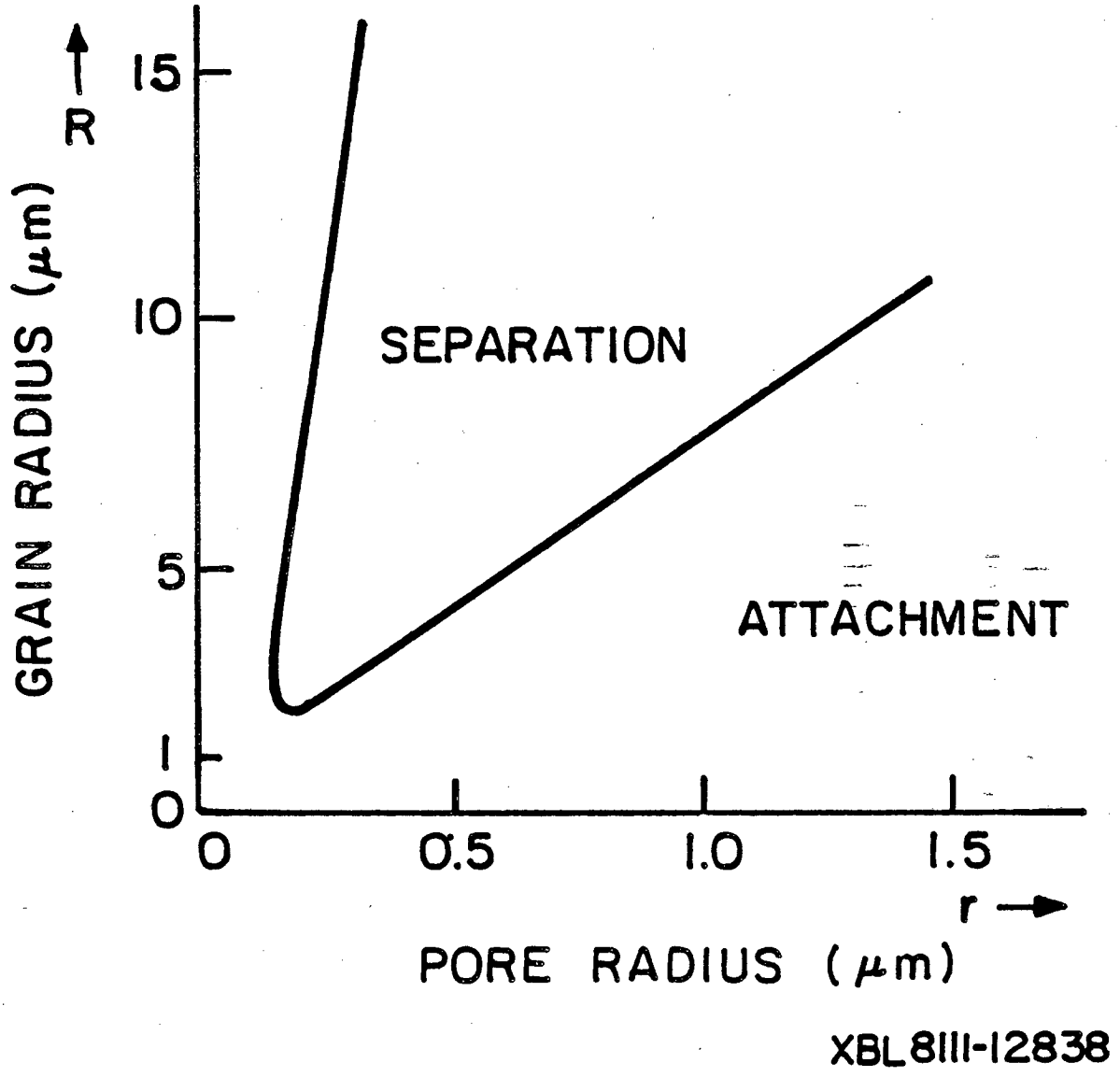
GRAIN RADIUS (μm)
R
15
10
5
1
0
SEPARATION
ATTACHMENT
0
0.5
1.0
1.5
r
PORE RADIUS (μm)
XBL8111-12838

FIG. 1

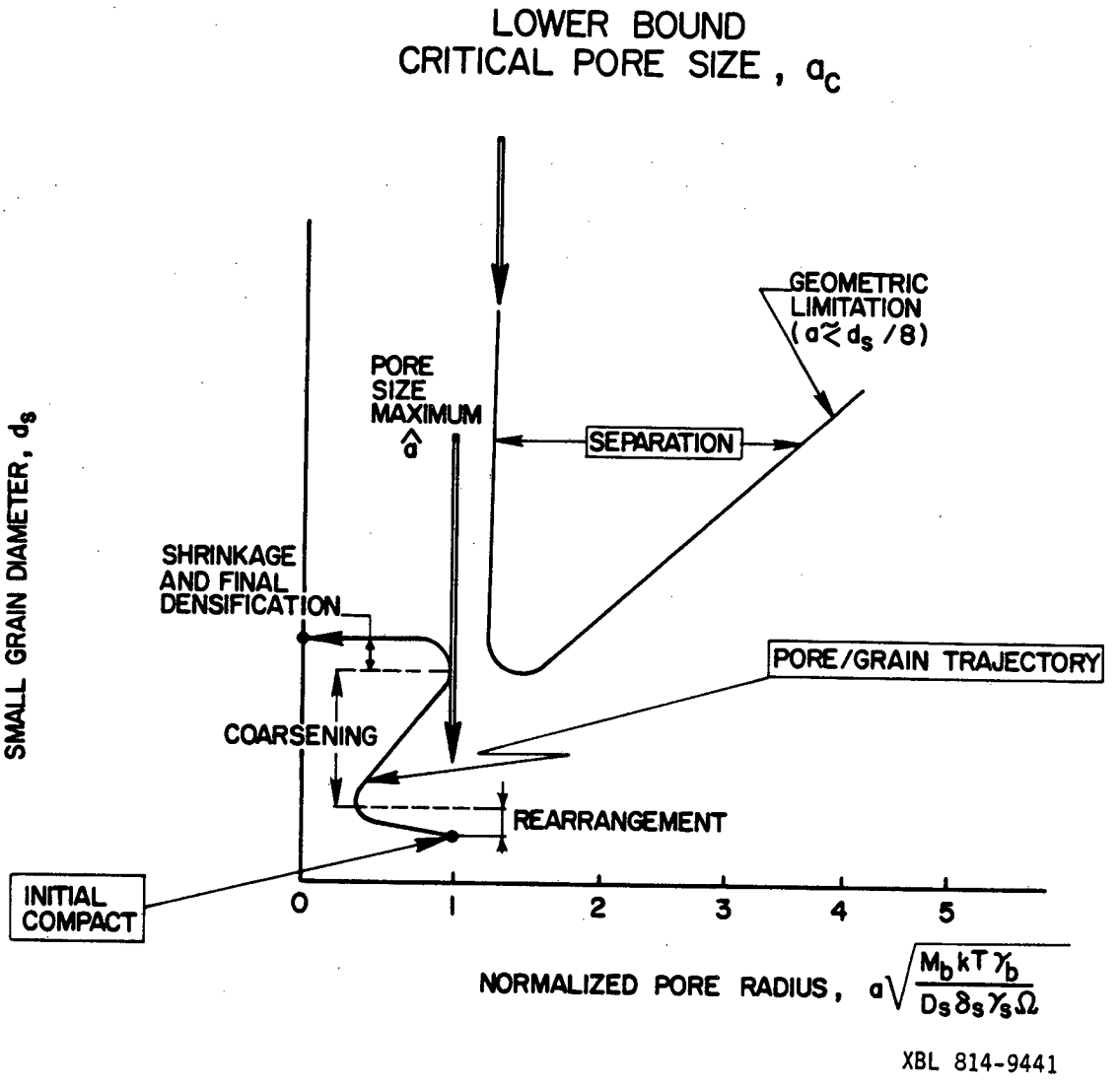
LOWER BOUND
CRITICAL PORE SIZE , a_c
GEOMETRIC LIMITATION ($a \gtrsim d_s/8$)
PORE SIZE MAXIMUM $\hat{a}$
SEPARATION
SHRINKAGE AND FINAL Ddensification
PORE/GRAIN TRAJECTORY
COARSENING
REARRANGEMENT
INITIAL COMPACT
SMALL GRAIN DIAMETER, d_s
0
1
2
3
4
5
NORMALIZED PORE RADIUS, $a\sqrt{\frac{M_b kT\gamma_b}{D_s\delta_s\gamma_s\Omega}}$
XBL 814-9441

FIG. 2

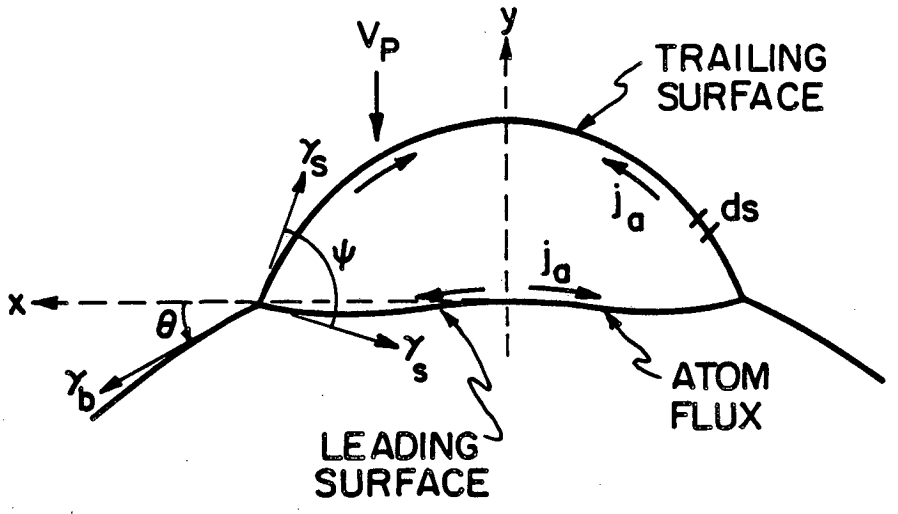

XBL 816-5972

FIG. 3

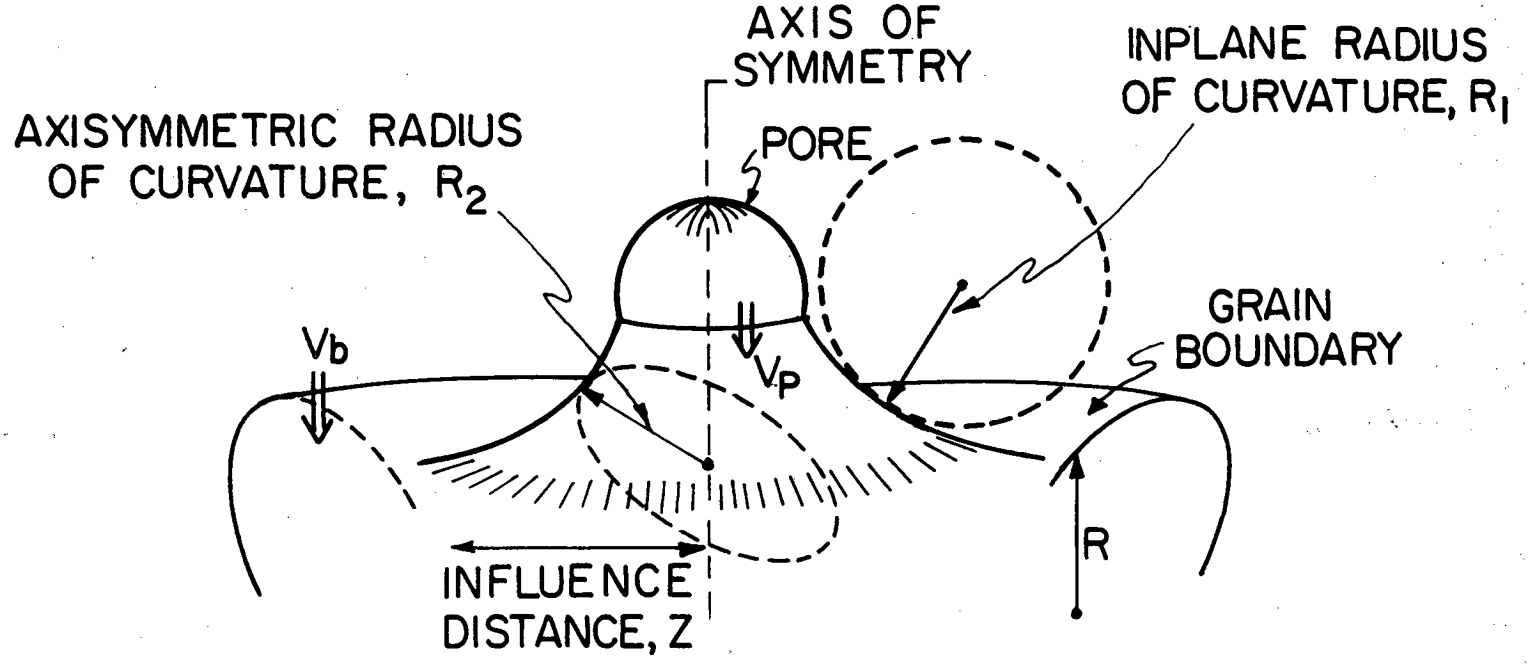
AXIS OF
SYMMETRY
INPLANE RADIUS
OF CURVATURE, R_1
AXISYMMETRIC RADIUS
OF CURVATURE, R_2
PORE
GRAIN
BOUNDARY
V_b
V_P
R
INFLUENCE
DISTANCE, Z
XBL816-5979

FIG. 4

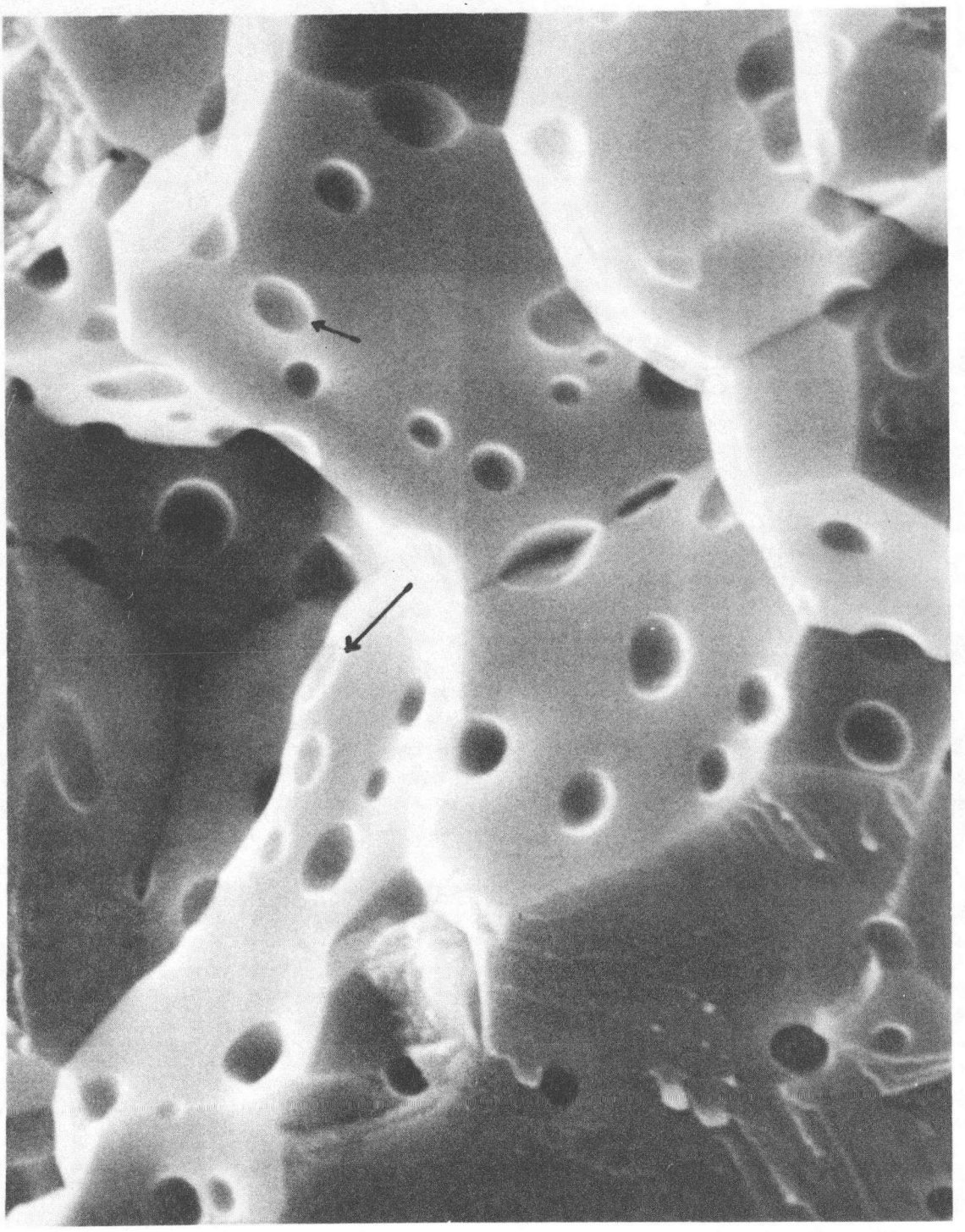

XBB 810-11236

FIG. 5

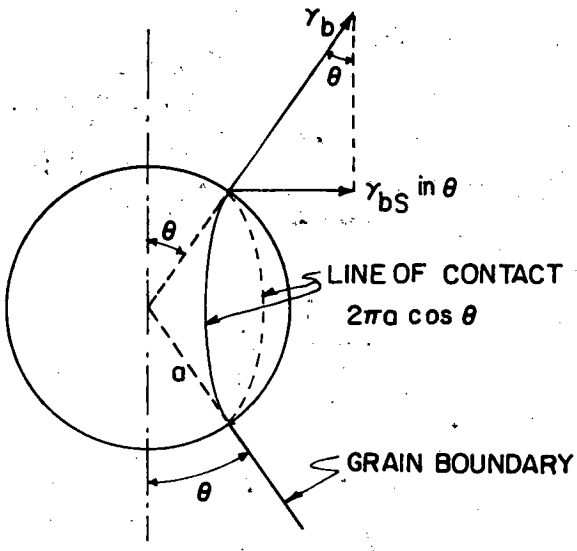
γ_b
θ
γ_{bS} in θ
θ
LINE OF CONTACT
$2\pi a \cos\theta$
a
GRAIN BOUNDARY
θ

FIG. 6

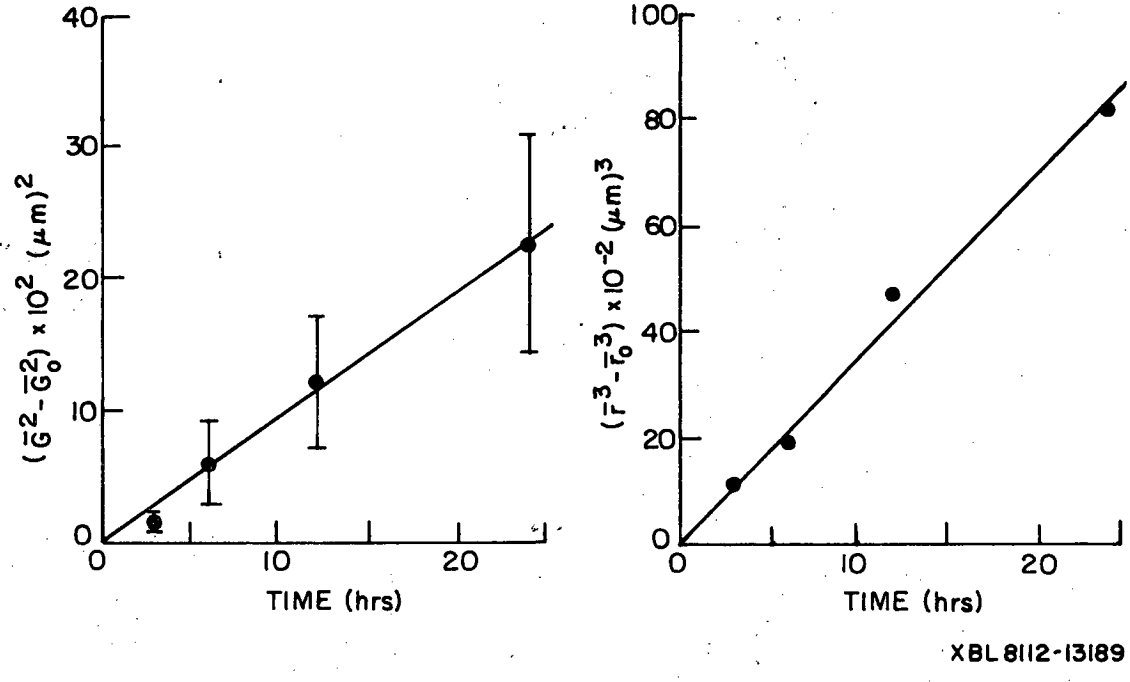
40
30
20
10
0
$(\bar{G}^2 - \bar{G}_0^2) \times 10^2$ $(\mu m)^2$
0
10
20
TIME (hrs)
100
80
60
40
20
0
$(\bar{r}^{-3} - \bar{r}_0^{-3}) \times 10^{-2}$ $(\mu m)^3$
0
10
20
TIME (hrs)
XBL 8112-13189

(a) (b)

FIG. 7

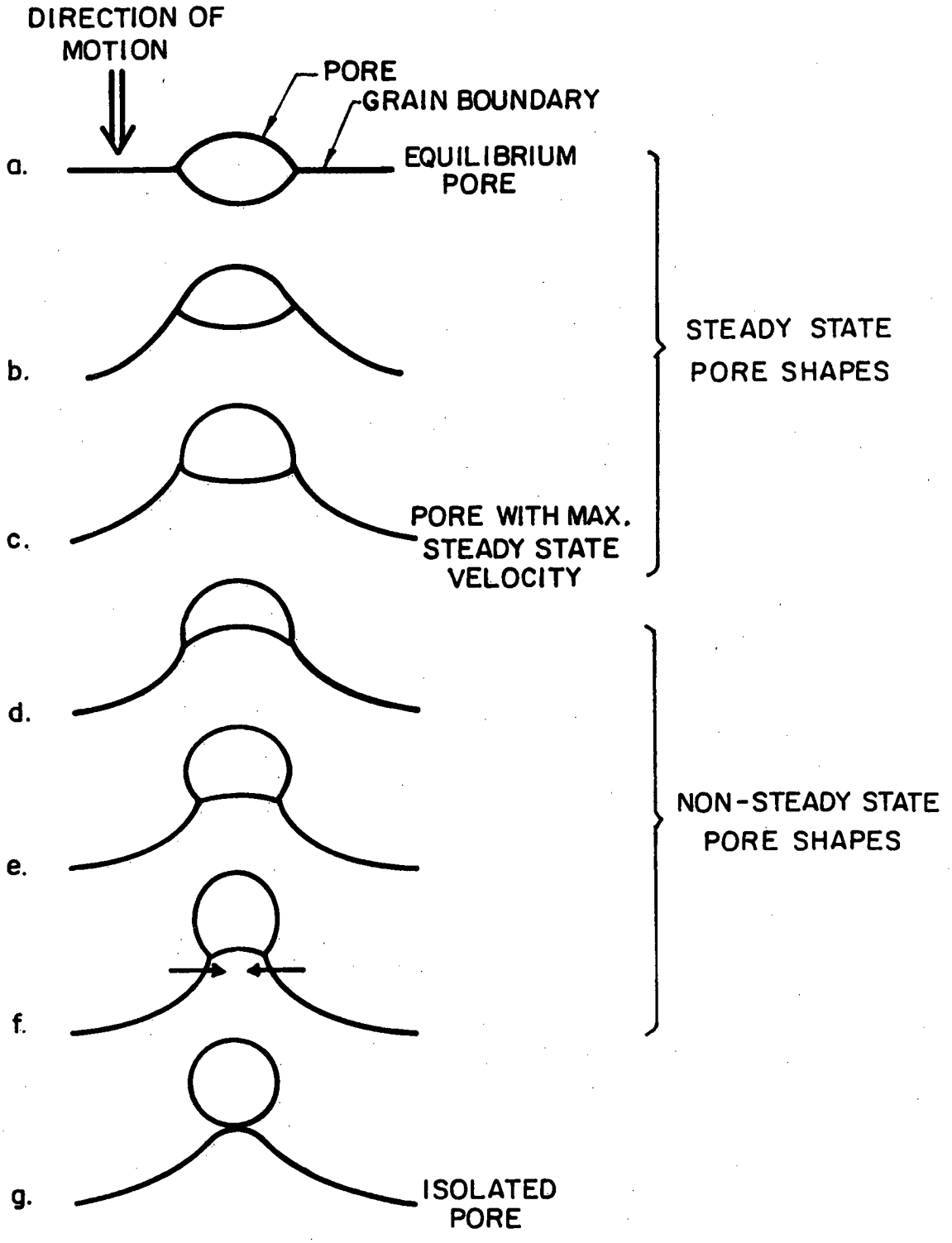
DIRECTION OF MOTION
PORE
GRAIN BOUNDARY
a.
EQUILIBRIUM PORE
b.
STEADY STATE PORE SHAPES
c.
PORE WITH MAX. STEADY STATE VELOCITY
d.
NON-STEADY STATE PORE SHAPES
e.
f.
g.
ISOLATED PORE
XBL 8111-12837

FIG. 8

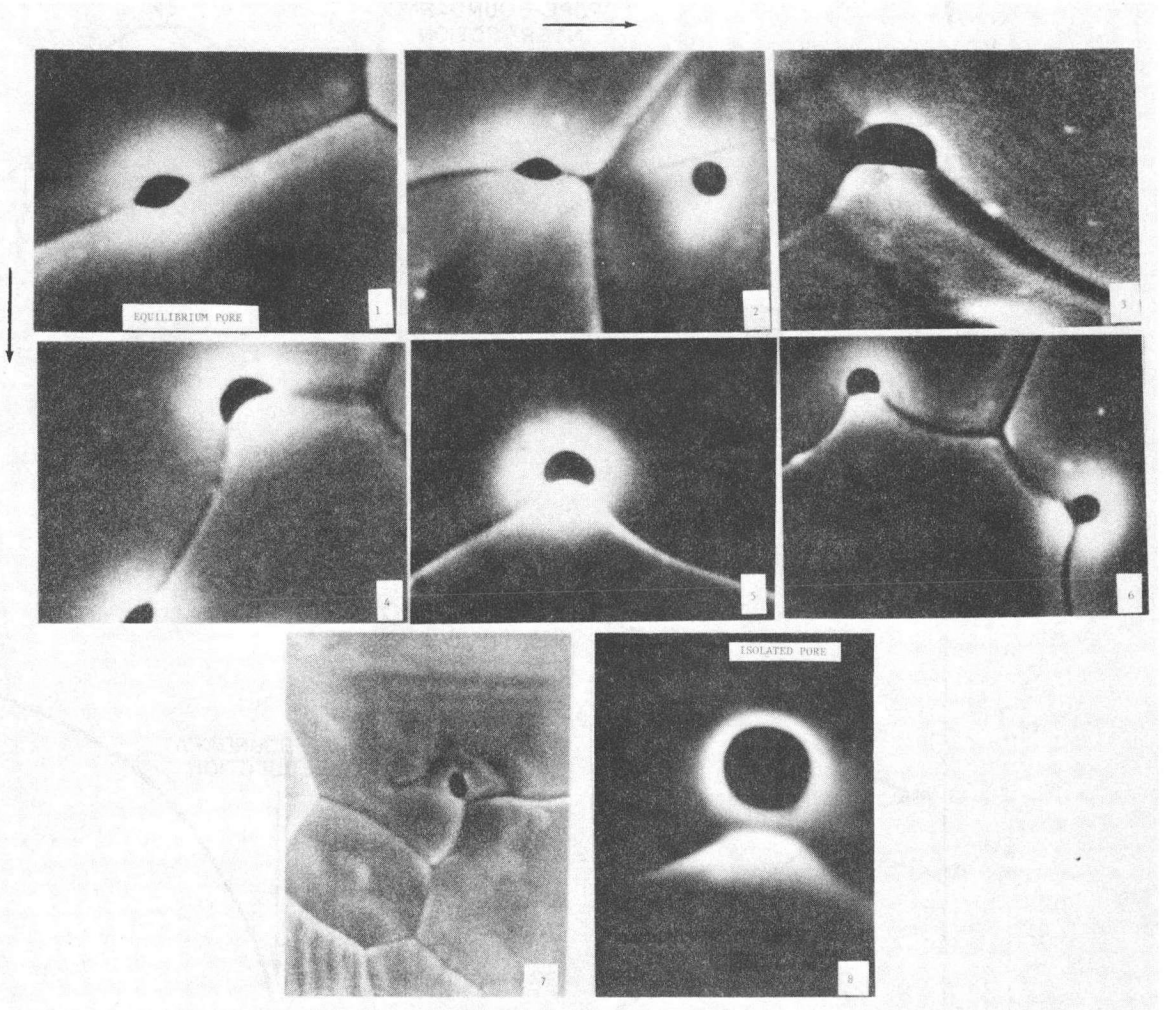

PORE SHAPES IN SEQUENCE DURING BREAKAWAY

XBB 810-10702

FIG. 9

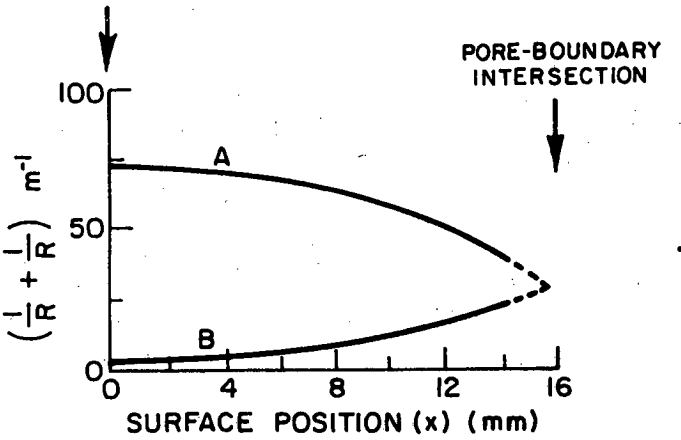

FIG. 10

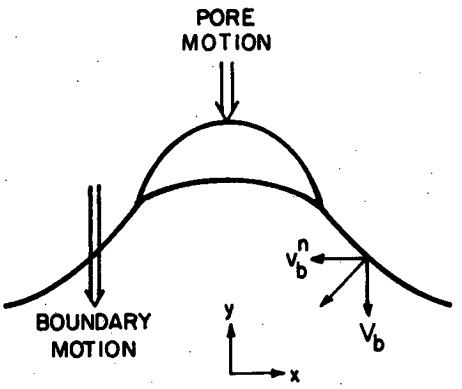

FIG. 11

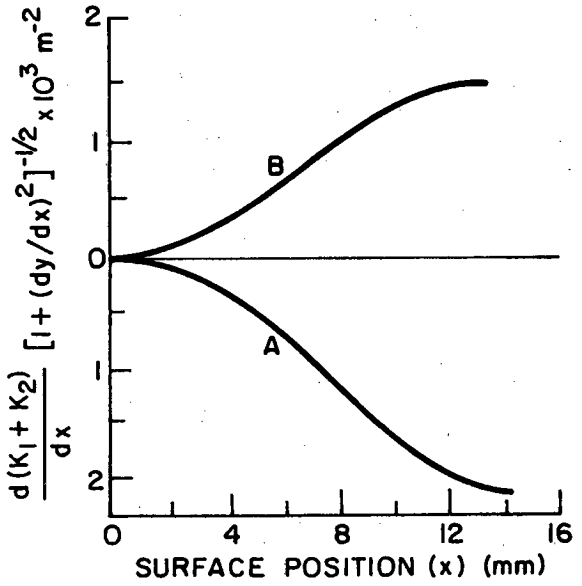

FIG. 12

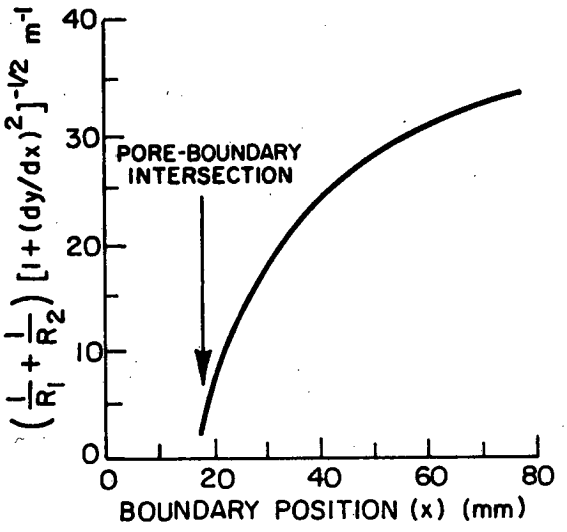

FIG. 13

XBL 8111-12839

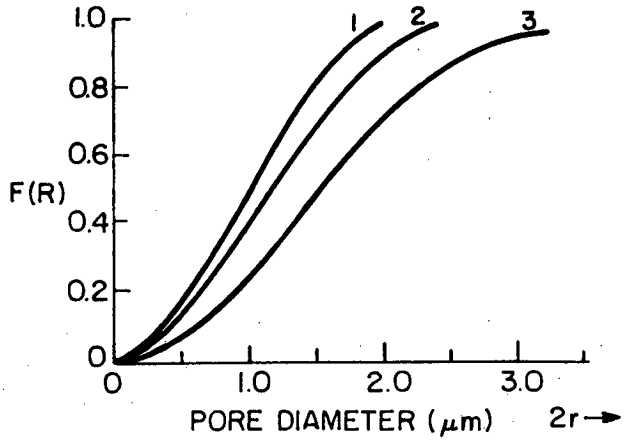

FIG. 14

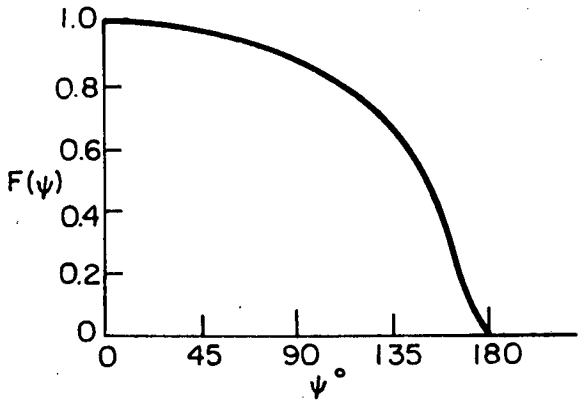

FIG. 15

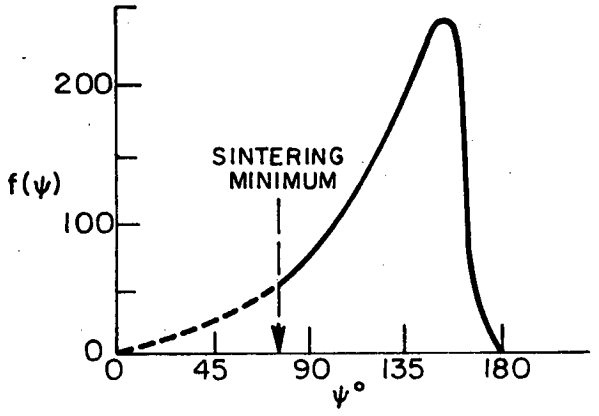

FIG. 16

XBL 8112-13159

TECHNICAL INFORMATION DEPARTMENT
LAWRENCE BERKELEY LABORATORY
UNIVERSITY OF CALIFORNIA
BERKELEY, CALIFORNIA 94720